

ACTIVE FLOW CONTROL AND THERMAL PROTECTION FOR A WING-BODY CONFIGURATION BASED ON LATERAL JET

Liaolei He[1], Fang Chen[1] & Yuqi Wei[1]

[1]School of Aeronautics and Astronautics, Shanghai Jiao Tong University, Shanghai 200240, China

Abstract

During the high-speed ascent and atmospheric re-entry of the reusable launch vehicle (RLV), aerodynamic heating occurs, which poses significant challenges to space transportation missions. The design of thermal protection systems is one of the cores related to flight economy and safety. This paper introduces an active thermal protection technology based on lateral jet and studies the influence of its parameters through steady and unsteady simulations. The results show that the heat flux at the leading edge changes nonlinearly when the pressure ratio of the jet increases from 0.02 to 0.20. When the pressure ratio is 0.16, the peak heat flux at the leading edge decreases by 31.5% and the average heat flux decreases by 76.8%. Compared with the case where the jet Mach number is equal to 1, an increase in the jet Mach number will reduce the impact of the jet on the original shock wave structure, resulting in an unsatisfactory thermal protection effect. Unsteady jets have a greater reduction in heat flux compared to steady jets during a certain period. In addition, a deep learning-based virtual sensor method aimed at inferring unknown physical data in a specific area is designed. The prediction results of the test set indicate that its error does not exceed 10%. By the approach proposed in this paper, the local peak of heat flux is weakened, which is beneficial for reducing the cost of the thermal protection system. The research in this paper provides a new perspective for active thermal protection methods and contributes to the complete reusable design of future vehicles.

Keywords: Aerothermal effects; Shock-shock interaction; Active thermal protection; Lateral jet; Deep learning

1. Introduction

The application scope of aircraft now extends beyond international transportation. In recent years, reusable launch vehicles (RLV) that can travel multiple times between the ground and space, such as the X-37B Orbital Test Vehicle, have attracted increasing attention. However, since the flight speed of the vehicle in the atmosphere reaches hypersonic speed, the aerothermal effect cannot be ignored. For wing-body assemblies, high heat flux density areas exist at the head and the leading edge of the wing. Prolonged and intense thermal loading in a localized region of the vehicle may result in irreversible structural damage. In particular, when the body bow shock and the leading edge shock occur shock-shock interactions (SSI), the peak heat flux on the leading edge of the wing/rudder can increase to 2-3 times of the original [1], which seriously endangers flight safety and affects service life. In some RLV designs, the wings can also serve as control surfaces. The starship produced by Space X, which is equipped with two pairs of wings/rudders at the front and rear, is a typical example. Thus, thermal protection of the leading edge of the wing/rudder is critical.

Before the concept of active thermal protection emerged, vehicles mainly used passive thermal protection. Passive thermal protection relies on expensive composite materials. In the current industry context where multiple round trips between low Earth orbit and the ground are required, passive thermal protection systems cannot be fully reusable and are often designed with excessive mass relative to mission requirements. Therefore, while continuing to optimize the materials of passive thermal

protection systems, researchers are committed to developing new research ideas for active thermal protection. Jet is one of the main methods to achieve active flow control and thermal protection. In 2005, Hayashi et al. achieved drag reduction and thermal protection of the blunt body through opposing jet [2]. In 2018, Guo et al. [3] analyzed the specific parameter effects of opposing jet in hypersonic flow. The results showed that the cost of achieving the best performance of opposing jet was relatively high. Ji et al. [4] proposed multiple opposing jets method for drag reduction and thermal protection over a waverider. The opposing jet directly opposes the high-speed incoming flow, while the direction of the lateral jet forms a certain angle with the incoming flow direction [5]. In 2023, the lateral jet and spike were combined for better drag reduction and thermal protection, and Wang et al. analyzed the combined shock wave control mechanism [6]. Some current studies indicate that the position of the jet, the orifice geometry [7], and the jet pressure [8] are key factors determining how the jet interferes with the flow field. In addition, Meng et al. [9] analyzed the drag reduction and heat reduction effects of porous lateral jets on the wings of hypersonic vehicles, and their active method achieved a performance improvement of approximately 20%. Jet technology is also applied in a V-shaped blunt leading edge [10] and rudder [11, 12], but neither of them takes into account the influence of body bow shock wave. Among existing studies, the momentum flux ratio of the jets tends to be relatively low, and the analyses predominantly focus on steady-state jets. In addition, after the rise of artificial intelligence (AI) research, a class of agent-based methods for automatically controlling the injection parameters of the jet was proposed to optimally perform flow control. One of the foundations of this idea is to provide the agent with sufficient observable information, but the number of sensors is always limited in practice. To address the aforementioned challenge, the predictive method based on deep learning, which predicts essential flow field data in other areas using a small amount of known sensor data, has been continuously developed since 2021 [13]. Currently, this type of methods is mainly applied in engine issues [14, 15].

This paper proposes to control shock-shock interactions with lateral jet for a wing-body configuration model, and analyzes the thermal protection effect and mechanism. Different simulation cases are designed to reveal the effects of pressure ratio and jet Mach number. Meanwhile, this study also investigates the unsteady thermal protection characteristics of pulsed jets, and the results demonstrate that such a method offers certain advantages over steady jets. Furthermore, this work proposes a deep learning-based virtual sensor method to underpin future intelligent active flow control. The rest of this paper is structured as follows: Sec. 2. describes our numerical methods, model parameters and neural network architecture in detail; and in Sec. 3., we present and discuss the simulation results and the performance of virtual sensors; finally, we conclude the paper in Sec. 4..

2. Methods

2.1 Numerical methods

The flow field data in this paper is derived from three-dimensional Reynolds-averaged Navier–Stokes (RANS) simulations. The three-dimensional unsteady compressible Navier–Stokes equation in the Cartesian coordinate system can be written as:

$$\frac{\partial Q}{\partial t}+\frac{\partial F}{\partial x}+\frac{\partial G}{\partial y}+\frac{\partial H}{\partial z}=\frac{1}{Re_{\infty}}\left(\frac{\partial F_v}{\partial x}+\frac{\partial G_v}{\partial y}+\frac{\partial H_v}{\partial z}\right) \tag{1}$$

where x, y, z are the spatial coordinates, t is the time, Re_{∞} is the Reynolds number. The conserved state variable Q, the convective flux vectors F, G, H, the diffusion flux vectors F_v, G_v, H_v are presented as follows:

$$Q=\begin{bmatrix}\rho\\ \rho u\\ \rho v\\ \rho w\\ \rho E\end{bmatrix},F=\begin{bmatrix}\rho u\\ \rho u^2+p\\ \rho uv\\ \rho uw\\ (\rho E+p)u\end{bmatrix},G=\begin{bmatrix}\rho v\\ \rho uv\\ \rho v^2+p\\ \rho vw\\ (\rho E+p)v\end{bmatrix},H=\begin{bmatrix}\rho w\\ \rho uw\\ \rho vw\\ \rho w^2+p\\ (\rho E+p)w\end{bmatrix},$$
$$F_v=\begin{bmatrix}0\\ \tau_{xx}\\ \tau_{xy}\\ \tau_{xz}\\ q_x+u_j\tau_{xj}\end{bmatrix},G_v=\begin{bmatrix}0\\ \tau_{xy}\\ \tau_{yy}\\ \tau_{yz}\\ q_y+u_j\tau_{yj}\end{bmatrix},H_v=\begin{bmatrix}0\\ \tau_{xz}\\ \tau_{yz}\\ \tau_{zz}\\ q_z+u_j\tau_{zj}\end{bmatrix} \tag{2}$$

$$E=e+\frac{1}{2}\left(u^2+v^2+w^2\right) \tag{3}$$

where u, v, w are the velocity components in the x, y, z directions, respectively; τ_{ij} is the stress in the j direction acting on a plane perpendicular to the i axis; p and ρ are the fluid pressure and density; the total energy E is defined by Eq. (3), and e represents the internal energy.
The heat flux is given by

$$q_x=\kappa\frac{\partial T}{\partial x},\ q_y=\kappa\frac{\partial T}{\partial y},\ q_z=\kappa\frac{\partial T}{\partial z}, \tag{4}$$

where κ is the thermal conductivity coefficient and T is the temperature. The main numerical methods used in this paper are presented as follows. The RANS control equations are solved using finite volume method. The AUSMDV flux splitting scheme is employed for discretizing the inviscid fluxes. Meanwhile, the LU-SGS implicit scheme is employed for time iteration. For the unsteady cases, dual time stepping is used, and the physical time step is set to $1\times10^{-7}s$. $k-\omega\ SST$ is the turbulence model in this study. The jet experimental data in Reference [16] are used to verify the numerical calculation method. As can be seen from Figure 1, the simulation results are basically consistent with the experimental data.

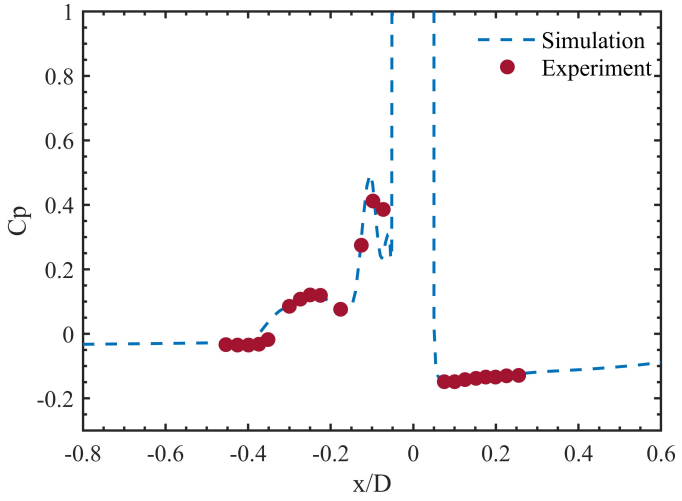


Figure 1 – Experimental data and simulation result.

2.2 Geometric parameters and different cases

The simplified geometric model of the front end of the RLV is shown in Figure 2. The diameter D of the jet hole is 4mm, and the distance from the jet hole to the leading edge is 10D. Other conditions are as follows: the flight altitude is 45km, the flight speed is Mach 12, and the temperature of the wall and the jet inlet are both 300K. Case 1 to Case 6: Pressure ratio PR= 0.02 to 0.2, jet Mach number M_j=1. Case 7 and Case 8: PR=0.16, M_j = 2 and 3. The model's grid is a structured grid, consisting

of 7.6 million cells, and the grid independence analysis is completed. The pressure ratio is defined as the ratio of the total pressure of the jet to the total pressure at point A in the flow field without the jet. Point A is located above the jet hole. The momentum flux ratio is defined as:

$$J = \frac{\rho_j U_j^2}{\rho_\infty U_\infty^2}, \tag{5}$$

where ρ_j and ρ_∞ represent the densities of the jet and incoming flow, respectively; U_j and U_∞ represent the velocities of the jet and incoming flow, respectively.

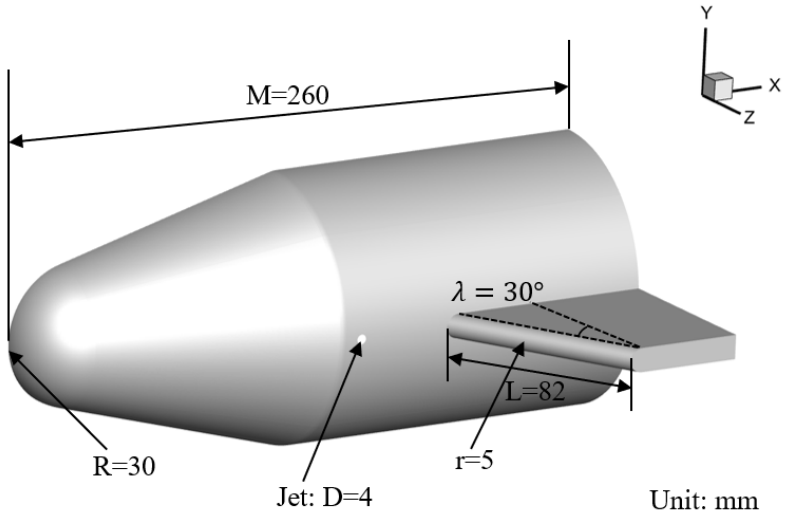


Figure 2 – The simplified geometric model.

2.3 Neural network architecture for virtual sensors

This paper aims to use a small amount of known data to infer unknown data in other regions. Due to the irregular distribution of the input points, the convolutional neural network (CNN) based on spatial convolution cannot handle this task in the same way as it does for other tasks [17]. Although the graph convolutional neural network (GNN) has overcome the limitations of the Cartesian grid, the limited and sparse data in this paper is not suitable as the input for GNN [18]. Neural operators such as DeepONet [19] can flexibly handle discrete coordinates, but the output and input of the neural operator must correspond to the same point in the function space. The Transformer architecture was first proposed in the field of natural language processing (NLP) to improve the extraction of long-distance connections for each word element in a sequence [20].

In recent years, there is a clear trend that more and more Transformers and their improved versions are being applied to spatio-temporal sequence prediction problems in other fields. The Transformer-based architecture proposed in this article is shown in Figure 3. The data of a total of R points on the aircraft surface are known, and the data of the other V points are predicted by virtual sensors (the neural network model). The input of the neural network model consists of the three-dimensional coordinates of $R+V$ points, as well as the pressure and heat flux data of R points at the current moment and the previous three moments. The main body of the model has two branches: the PointNet branch, which converts the three-dimensional coordinates into high-dimensional latent codes to obtain geometric information, and ultimately this branch yields a $L1$ of length 128; the Transformer branch, which inputs the physical variables into the stacked Transformer layers to obtain the spatial and temporal connections of the known data, and ultimately this branch yields a $L2$ of length 128. $L1$ and $L2$ are stacked and then input into the final part of the neural network, thereby obtaining the predicted value as the output. The core of the proposed architecture lies in extracting the temporal and spatial relationships of physical variables and integrating them with geometric information, thereby facilitating the prediction of pressure and heat flux at the target points.

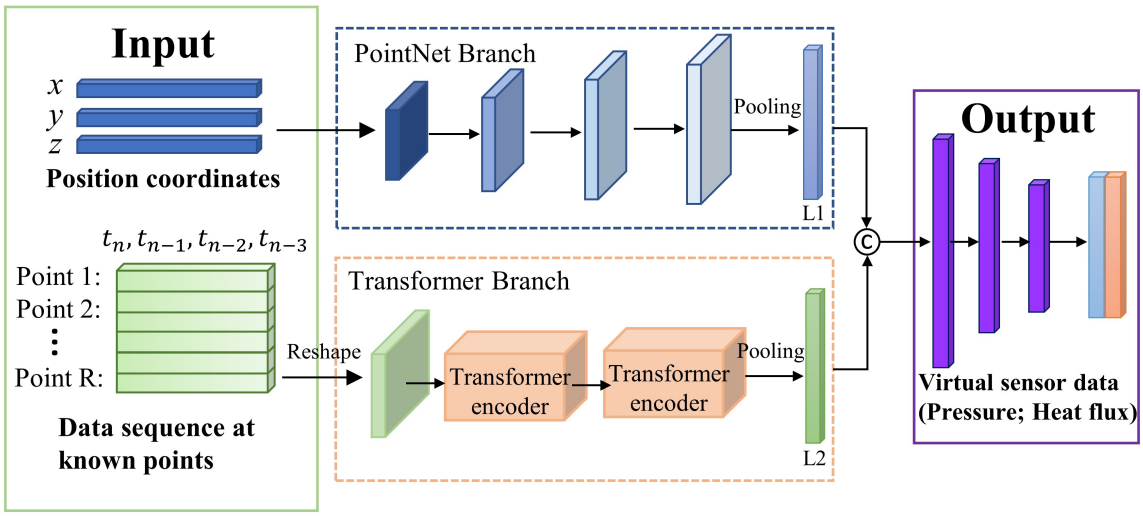


Figure 3 – The neural network architecture.

3. Results and Discussion

3.1 The effect of different pressure ratios

As shown in Figure 4, Type V shock-shock interference (SSI) is triggered when the body bow shock intersects the leading edge shock, which in turn causes extremely high aerothermal loads on the leading edge. In Cases 1 to 6, lateral jets with different pressures are used to mitigate the SSI, thereby achieving a reduction in heat flux. As the pressure ratio increases, the influence of the jet on the flow field structure becomes increasingly evident, as shown in Figure 5. The size of the expansion zone of the jet is positively correlated with the pressure ratio, especially within the pressure ratio range of 0.02 to 0.08. It can be seen that the jet wake and the jet bow shock wave act at the leading edge, replacing the direct intersection of the body bow shock wave and the leading edge. The momentum flux ratio will be relatively large due to the low-density air at high altitudes, as shown in formula 5. According to classical theory, the jet penetration height increases with an increase in the momentum flux ratio, which is beneficial for the intervention effect of the jet. Figure 6 shows the heat flux and pressure coefficient on the centerline of the leading edge. With the increase of pressure ratio, the overall heat flux and the pressure coefficient are significantly decreasing. As the position of the peak moves towards the wingtip, the pattern also changes: single peak - double peak - single peak. The specific values are recorded in Table 1. All jet with different pressure ratios are highly effective in providing thermal protection for the wing root and the junction between the wing and the fuselage. Meanwhile, the average heat flux is steadily decreasing as the pressure ratio increases. It is noteworthy that when PR equals 0.02, the maximum heat flux exhibits an "unexpected" increase of 2.2%. Furthermore, the increase in pressure ratio does not lead to a significant reduction in the maximum heat flux until the pressure ratio rises a certain value. When PR reaches 0.16, the peak heat flux on the leading edge decreases by 31.5%, and the average heat flux drops by 76.8%. A small high heat flux area will also appear on the wall in front of the jet due to flow separation. When the pressure ratio is very high, the heat flux in this area can even reach half of the heat flux at the stagnation point, indicating that a high pressure ratio can also be detrimental to overall thermal protection.

One of the main reasons for the decrease of heat flux is that the bow shock generated by the jet withstands the original body bow shock. As shown in Figure 7, taking case 4 as an example, due to the "lifting" effect of the jet, the original Type V SSI has been transformed into two relatively weak Type VI SSI. The influence of the jet on the leading edge can be roughly divided into three sections: upper, middle and lower. The lower end is mainly affected by the recirculation zone. The middle section is directly affected by the cold jet and corresponding vortices. The upper section is affected by multiple shock waves, expansion waves and the shear layer on the windward surface of jet. The primary favorable factors contributing to the suppression of extremely high heat flux by jets are as follows:

Firstly, the shock-shock interaction (SSI) induced by the jet bow shock waves and leading-edge shock waves is weaker, attributable to the intensity and angle of these shock waves. Secondly, the mixing occurs between the low-enthalpy jet and the high-enthalpy incoming flow within the jet shear layer. However, these can't explain the increase in the maximum heat flux when PR is 0.02. Indeed, when the PR is relatively low, the lateral jet with a density several dozen times greater than that of the incoming flow will "obstruct" the incoming flow, causing the high-enthalpy airflow to converge towards the upper section of the wing, thereby exacerbating heat conduction. The phenomenon, wherein the gas density between the bow shock wave and the jet increases by over 10% in comparison to the case without the jet, also underscores this point. One of the more fundamental reasons is that the shear layer of the jet has inconsistent transport velocities for momentum and energy in this situation. In summary, during the rise of pressure ratio, all favorable and unfavorable factors jointly influence the flow field, resulting in a nonlinear change in maximum heat flux.

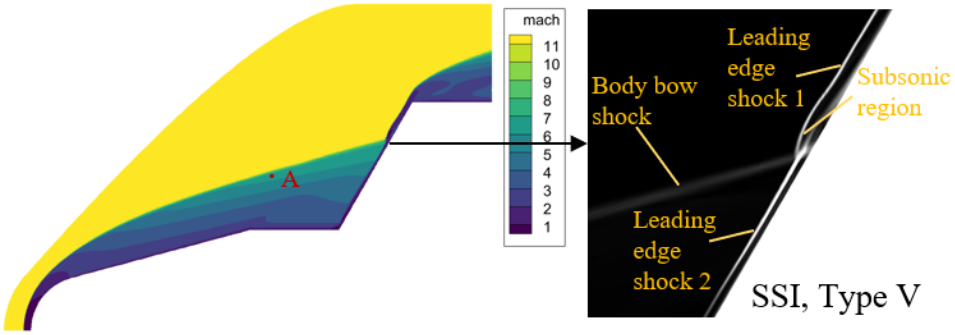


Figure 4 – Diagram of flow field without jet.

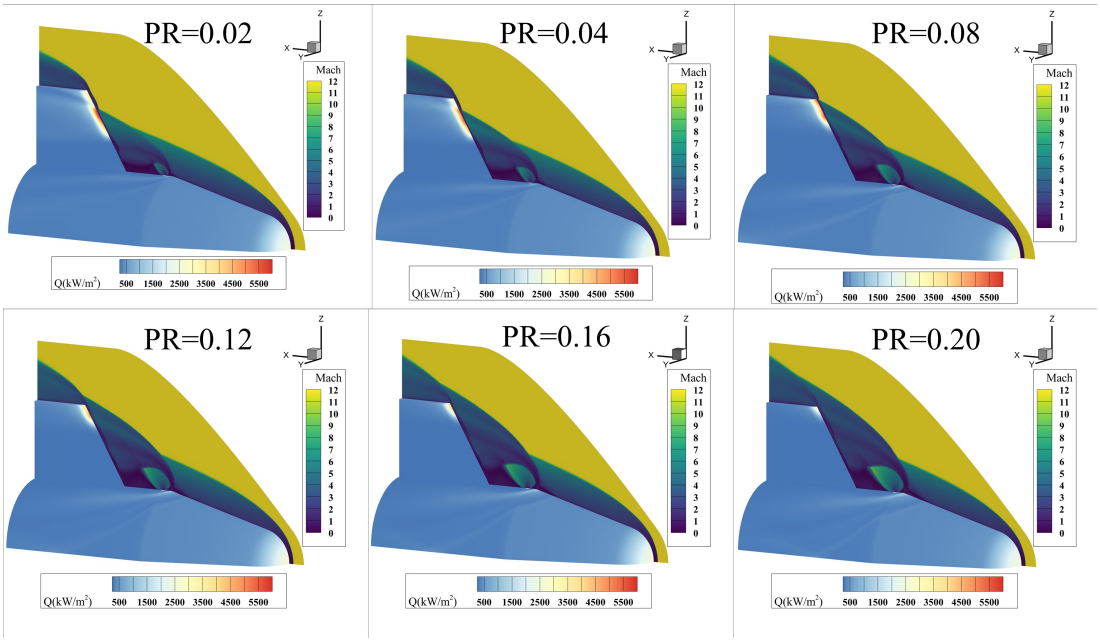


Figure 5 – Diagram of flow field with different jets.

Table 1 – Comparison of thermal protection effects of different PR.

Case	PR	Momentum flux ratio J	Pattern	Peak of heat flux(kW/m^2)	Decline of the maximum	Decline in average
1	0.02	2.31	single peak	5938	-2.2 %	33.8 %
2	0.04	4.63	double peaks	5405 & 5532	4.8 %	40.2 %
3	0.08	9.26	double peaks	5561 & 5468	4.3 %	49.6 %
4	0.12	13.89	Approximately single peak	4255 & 4780	17.8 %	65.2 %
5	0.16	18.52	single peak	3985	31.5 %	76.8 %
6	0.2	23.15	single peak	3271	43.7 %	87.3 %

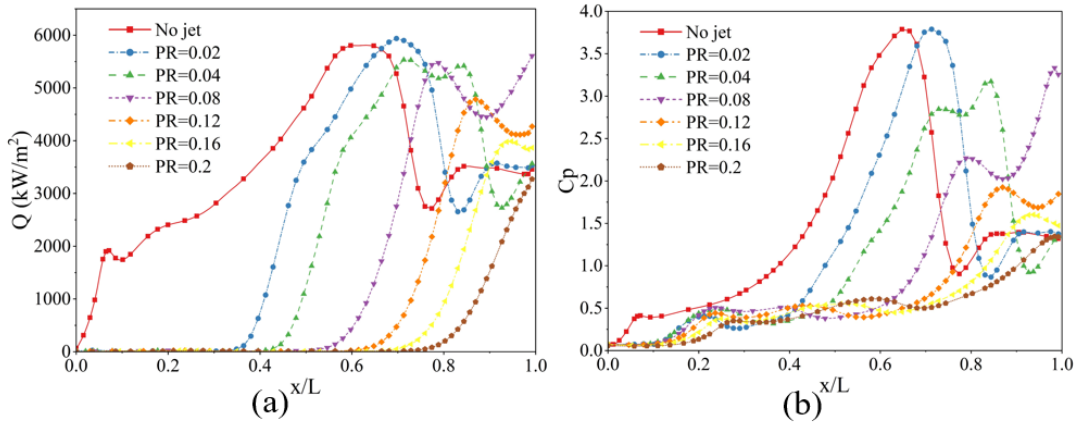


Figure 6 – The distribution of heat flux and pressure coefficient along the centerline of the leading edge.(a) heat flux (b) pressure coefficient

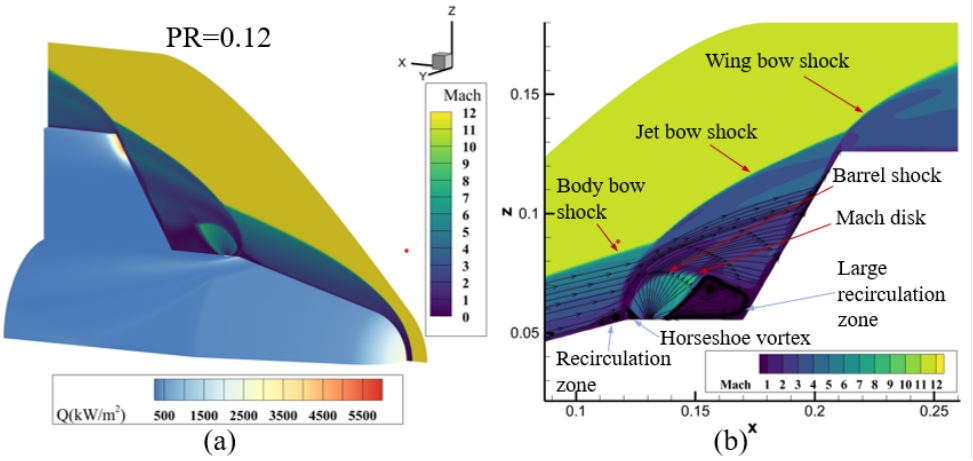


Figure 7 – The results of the Case 4.(a) global heat flux distribution (b) streamline

3.2 The effect of different jet Mach numbers

We also investigated the effect of different jet Mach numbers under the same pressure ratio (PR=0.16). The results of the flow field and surface heat flux are presented in Figure 8. From left to right, the jet Mach numbers are 1, 2 and 3. As the Mach number of the jet increases, the expansion zone of the jet becomes narrower, although the penetration height of the jet remains basically unchanged. Meanwhile, the size of the high heat flux area in the result of case 8 (Mach 3) is significantly larger than that of case 5 (Mach 1). For the thermal protection of the wing root, as the jet Mach number increases, the large recirculation zone will gradually be destroyed. For the leading edge of the upper section, detailed data are presented in Figure 9. The heat flux reduction performance of case 8 is even worse than that of case 4 (PR=0.12). In conclusion, the results of case 7 and 8 show that increasing the jet Mach number will weaken the influence of jet on the original shock wave train.

3.3 Dynamic characteristics of unsteady jet

In this paper, the effect of pulsed jet with pressure ratio jumping from 0.08 to 0.12 on thermal protection is investigated through unsteady simulation. The impact of pulsed jet can be divided into four stages: development stage, overshoot stage, oscillation stage and stable stage. Figure 10 shows the time series of the heat flux and pressure coefficient at a point on the leading edge. The entire process lasts for 350 microseconds, during which a significantly lower heat flux can be observed. According to the comparison of the images, it can be seen that the heat reduction effect of the jet in the range of 70 to 80 microseconds is significantly better than that of the final stable flow field. During this period, the maximum heat flux value even approaches the result of the steady jet with a pressure ratio of

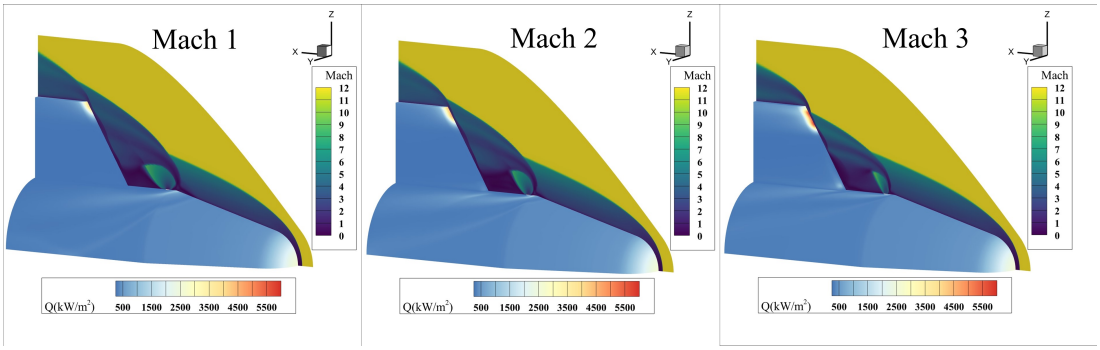


Figure 8 – The flow field and surface heat flux for different jet Mach numbers.

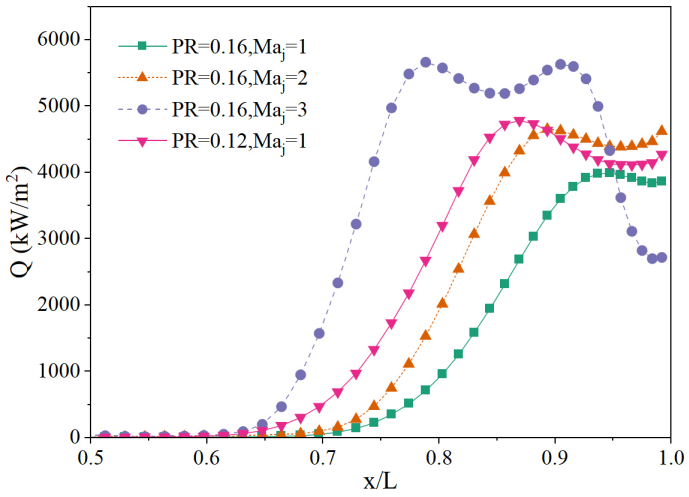


Figure 9 – The distribution of heat flux along the centerline of the leading edge.

0.20. The impressive fluctuations in heat flux and pressure are essentially attributed to the changes in shock waves and vortices in the unsteady flow field. During the evolution of the unsteady flow field, we observed that the contours of Mach disk and barrel shock wave expand along the flow direction. Simultaneously, the mixing between the low-temperature jet and the high-temperature incoming flow is also enhanced. These phenomena will ultimately diminish following a period of oscillation; however, certain transient flow characteristics can be utilized to improve the heat reduction effect and efficiency. The results of the unsteady numerical simulations demonstrate that pulsed jets can provide superior thermal protection compared to steady jets by utilizing unsteady flow effects. This finding indicates the potential for optimizing thermal protection performance through active control of unsteady jet.

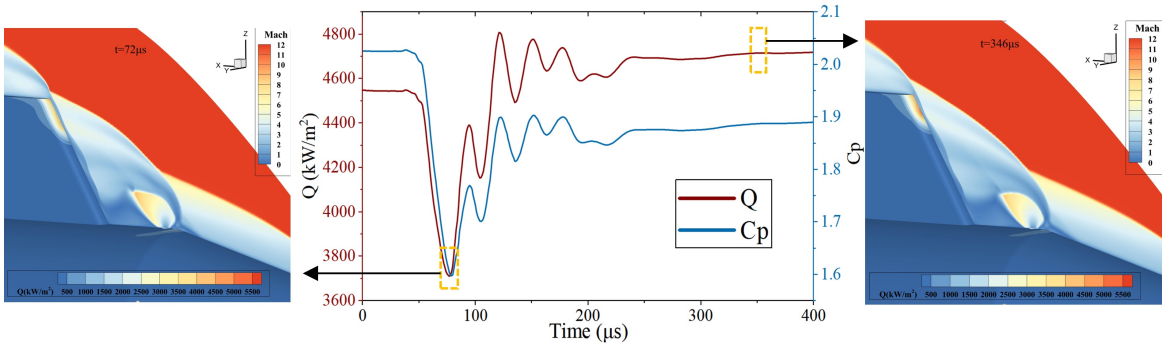


Figure 10 – Heat flux and pressure coefficient time series at a point on the leading edge.

3.4 The performance of virtual sensors

The implementation of intelligent active flow control requires a lot of sensors, however, it is not practical to deploy all the required sensors on the aircraft. Therefore, this paper proposes a virtual sensor method based on neural networks. The number of known data points, denoted as R, is 35, and the number of prediction points (virtual sensors), denoted as V, is also 35. Their distribution is illustrated in Figure 11, where blue squares represent known points and yellow squares represent virtual sensors. The known points are primarily distributed across the fuselage, whereas the virtual sensors are more extensively positioned on the wing. This design consideration stems from the engineering fact that sensor installation is more feasible on the fuselage than on the wings or rudder. Use the aforementioned unsteady jet case as the dataset to train and test the virtual sensor model. First, convert the pressure into pressure coefficient, convert the heat flux into dimensionless heat flux (divide the original data by the heat flux at the stagnation point), and then perform other pre-processing. The pre-processing of the data is beneficial for the training of the neural networks.

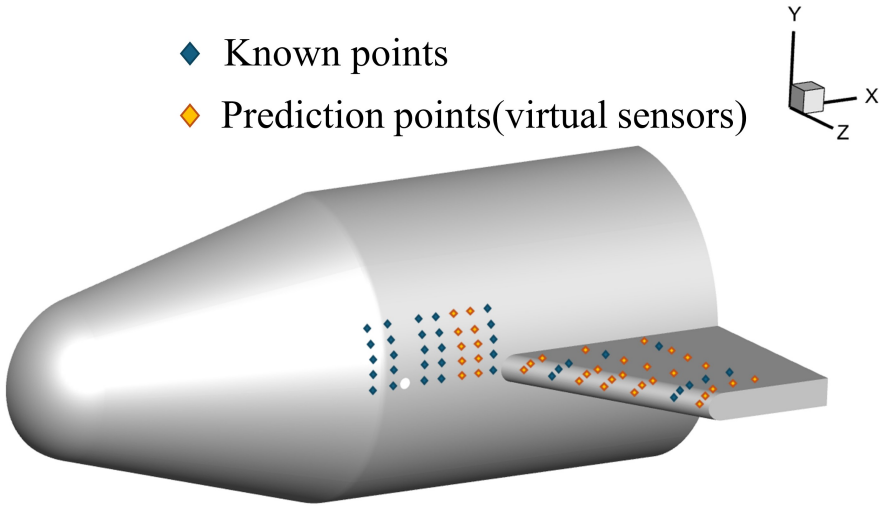


Figure 11 – Sensor distribution map.

In order to study the influence of the number of virtual sensors, a comparative experiment is designed in this paper. R remains unchanged, and the number of virtual sensors V is 7, 14, 21, 28, and 35 respectively. For each case, the number of learnable parameters of the neural network is the same, and each training is independent of the others. The loss curves of all neural networks eventually converge. The absolute relative errors of the test set for each situation are presented in Figure 12. The cross mark indicates abnormal samples. As observed from the box plot, the conclusion that an increase in the number of predicted points generally leads to greater errors does not hold true in this sparse prediction scenario. From the overall trend, the relative error of prediction gradually decreases with the increase of the number of virtual sensors. When V is 35, the average relative error of pressure and heat flux is 5%, and the maximum relative error is about 10%; When V is 7, the average relative error of pressure and heat flux is about 15%, and the maximum relative error exceeds 30%, which is unacceptable. We notice that a limited number of samples demonstrated high accuracy when V equaled 7 or 14, although there are also many high error outliers. This phenomenon indicates that the number of virtual sensors actually affects not the upper limit of the model's prediction accuracy but rather the robustness of the prediction. When the number of virtual sensors is sufficient, the predictive ability of the model will become stable. The prediction error of heat flux is basically consistent with that of pressure, and the former is slightly higher than the latter.

According to the introduction of neural network models in section 2.3, a too small number of virtual sensors is detrimental to the learning of geometric information and spatiotemporal features of physical variable sequences in the two branches of the model. In other words, the extraction of the overall latent features depends on a sufficient number of virtual sensors. The architectural design of the model to some extent explains that the prediction of pressure and heat flux becomes accurate and

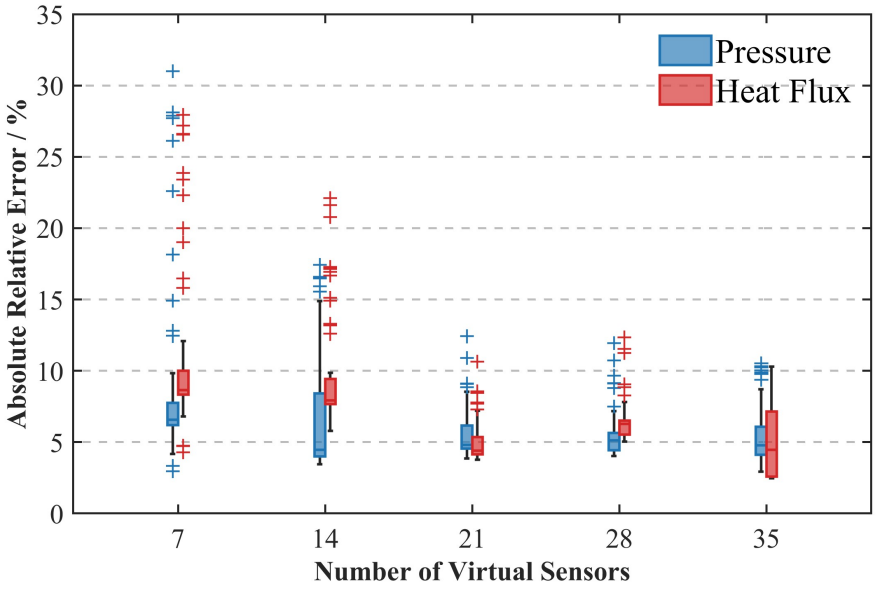


Figure 12 – Box plot of the relative errors of the samples in the test set.

robust when V approaches R. However, when V increases to several times that of R, the predictive ability of the model may reach its limit, causing the errors to gradually increase again. A sample from the test set is selected to visualize the prediction results, as shown in Figure 13. All the points are projected onto the x-z plane. The yellow circles represent the actual values, and the red squares represent the predicted values. Most of the squares and circles overlap each other, which indicates good predictions. The maximum deviation between the prediction and the true value occurs at the peak of pressure or heat flux. Specifically, for this sample, the virtual sensor underestimates the peak pressure and peak heat flux by 6.2% and 6.6%, respectively. In addition, the trained model (V=35) is transferred to another similar unsteady jet case. The average error of the prediction results increases to 11% in the new case, indicating that the model has generalization capacity to some extent. To conclude, this subsection illustrates the predictive performance of virtual sensors and analyzes their regularities.

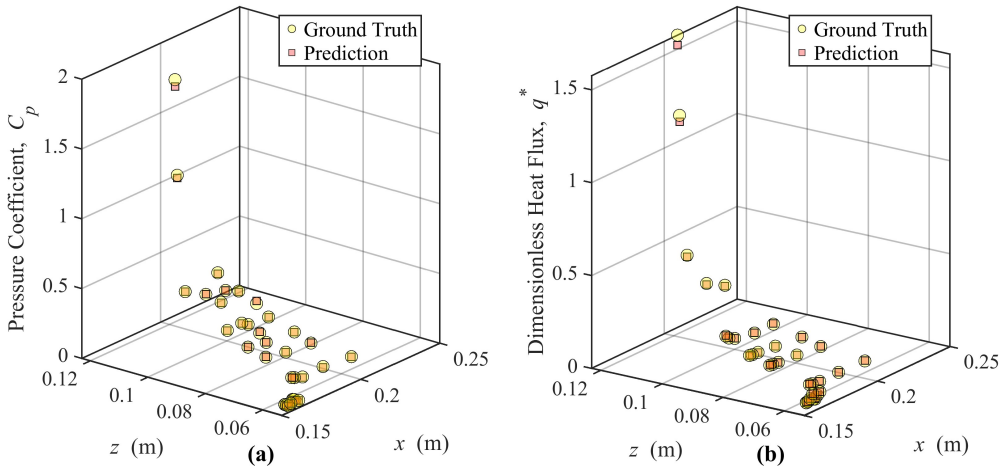


Figure 13 – Three-dimensional visualization of the prediction results.(a) Pressure coefficient (b) Dimensionless heat flux

4. Conclusions and Prospects

This study proposes an active thermal protection technology based on lateral jet for a wing-body configuration model. The numerical simulation results show that the jet can successfully control the shock wave structure. In order to infer the pressure and heat flux of points in other regions based on a small amount of known data, a virtual sensor method based on Transformer is developed. The major conclusions are drawn as follows. First, with the increase of jet pressure ratio, the heat flux distribution will change nonlinearly. Jets with different pressure ratios all provide excellent thermal protection for the wing root. The average heat flux gradually decreases as the pressure ratio increases. When the pressure ratio reaches 0.04, the jet begins to weaken the maximum heat flux; When the pressure ratio reaches a certain value between 0.12 and 0.16, the maximum heat flux begins to decline significantly. The results of the jet with a pressure ratio of 0.16 show that the peak heat flux on the leading edge decreases by 31.5%, and the average heat flux decreases by 76.8%. Second, the simulation results for different jet Mach numbers show that increasing the jet Mach number will reduce the impact of the jet on the original shock wave structure, resulting in unsatisfactory thermal protection performance. Third, the thermal protection effect of pulsed jets is superior to that of steady jets. The heat flux and pressure undergo a transient decline to significantly reduced levels, attributable to the dynamic evolution of shock waves and vortical structures. Fourth, when the number of virtual sensors V approaches the number of known points R, the model's predictions for pressure and heat flux will become accurate and robust. The average absolute relative error of the predictions for the samples in the test set is 5%, and the maximum absolute relative error is approximately 10%.

In future research, the influence of flow field modes generated by unsteady jets on surface pressure and heat flux should be more comprehensively and deeply studied. Additionally, the neural network-based virtual sensor method requires enhancement of its noise immunity, taking into account the inevitable noise in the flow field data for future applications.

5. Contact Author Email Address

Fang Chen: fangchen@sjtu.edu.cn

6. Copyright Statement

The authors confirm that they, and/or their company or organization, hold copyright on all of the original material included in this paper. The authors also confirm that they have obtained permission, from the copyright holder of any third party material included in this paper, to publish it as part of their paper. The authors confirm that they give permission, or have obtained permission from the copyright holder of this paper, for the publication and distribution of this paper as part of the ICAS proceedings or as individual off-prints from the proceedings.

References

[1] Michelle L. Mason and Scott A. Berry. Global Aeroheating Measurements of Shock–Shock Interactions on Swept Cylinder. *Journal of Spacecraft and Rockets*, 53(4):678–692, 2016.

[2] Kentaro Hayashi, Shigeru Aso, and Yasuhiro Tani. Numerical Study of Thermal Protection System by Opposing Jet. In *43rd AIAA Aerospace Sciences Meeting and Exhibit*, Reno, Nevada, 2005.

[3] Jinghui Guo, Guiping Lin, Xueqin Bu, Lizhan Bai, and Yanmeng Chao. Parametric study on the heat transfer of a blunt body with counterflowing jets in hypersonic flows. *International Journal of Heat and Mass Transfer*, 121:84–96, 2018.

[4] Chen Ji, Bing Liu, Wei Huang, Shi-bin Li, Zhao-e Meng, Li Yan, and Gautam Choubey. Design exploration on the drag reduction and thermal protection over a blunted waverider with multiple opposing jets. *Aerospace Science and Technology*, 124:107519, 2022.

[5] Anthony Techer, Yann Moule, Guillaume Lehnasch, and Arnaud Mura. Mixing of fuel jet in supersonic crossflow: Estimation of subgrid-scale scalar fluctuations. *AIAA Journal*, 56(2):465–481, 2018.

[6] Zekang Wang and Xiaobing Zhang. Research on a novel combined shock control mechanism for thermal protection and drag reduction in hypersonic compressible flow field. *International Journal of Heat and Mass Transfer*, 201:123592, 2023.

[7] Ravichandra Srinivasan and Rodney D. W. Bowersox. Simulation of transverse gaseous injection through diamond ports into supersonic freestream. *Journal of Propulsion and Power*, 23(4):772–782, 2007.

[8] A. T. Sriram and Joseph Mathew. Numerical simulation of transverse injection of circular jets into turbulent supersonic streams. *Journal of Propulsion and Power*, 24(1):45–54, 2008.

[9] Yu-shan Meng, Zhong-wei Wang, Yang Shen, Wei Huang, Yao-bin Niu, and Li Yan. Drag and heat reduction mechanism induced by jet interaction over a reusable launch vehicle in hypersonic flows. *Acta Astronautica*, 198:502–520, 2022.

[10] Shuai Li, Chao Yan, Dake Kang, Sijia Liu, and Zhenhua Jiang. Investigation of flow control methods for reducing heat flux on a V-shaped blunt leading edge under real gas effects. *Physics of Fluids*, 35(3):036113, 2023.

[11] Yi Zhou, Zhenbing Luo, Qiang Liu, Yan Zhou, and Wei Xie. Effect of rudder efficiency of high-speed aircraft subject to high-energy jet. *Physics of Fluids*, 36(12):125137, 2024.

[12] Yuan Feng, Dundian Gang, Qi Mi, Shikang Chen, and Zhiyao Yang. Numerical research and experiment on the thermal protection characteristics of opposing jets for rudder leading edge. *Physics of Fluids*, 37(7):076121, 2025.

[13] Yunfei Li, Ziao Wang, Weiyu Jiang, Zongqi Xie, Chen Kong, and Juntao Chang. Research on time sequence prediction of the flow field structure of supersonic cascade channels in wide range based on artificial neural network. *Physics of Fluids*, 34(1):016106, 2022.

[14] Chen Kong, Ziao Wang, Yunfei Li, and Juntao Chang. A deep learning approach for velocity field prediction in a scramjet isolator from schlieren images. *Chinese Journal of Aeronautics*, 36(11):58–70, 2023.

[15] Ye Tian, Yitong Zhao, Xue Deng, Maotao Yang, Erda Chen, Mengqi Xu, and Hu Ren. An intelligent prediction method for supersonic flow field in scramjet isolator enhanced by feature details. *Aerospace Science and Technology*, 161:110116, 2025.

[16] Patrick Gnemmi and Hans Schäfer. Experimental and Numerical Investigations of a Transverse Jet Interaction on a Missile Body. In *43rd AIAA Aerospace Sciences Meeting and Exhibit*, Reno, Nevada, 2005.

[17] Nils Thuerey, Konstantin Weißenow, Lukas Prantl, and Xiangyu Hu. Deep learning methods for reynolds-averaged navier–stokes simulations of airfoil flows. *AIAA Journal*, 58(1):25–36, 2020.

[18] Jiang-Zhou Peng, Yue Hua, Yu-Bai Li, Zhi-Hua Chen, Wei-Tao Wu, and Nadine Aubry. Physics-informed graph convolutional neural network for modeling fluid flow and heat convection. *Physics of Fluids*, 35(8):087117, 2023.

[19] Lu Lu, Pengzhan Jin, Guofei Pang, Zhongqiang Zhang, and George Em Karniadakis. Learning nonlinear operators via DeepONet based on the universal approximation theorem of operators. *Nature Machine Intelligence*, 3(3):218–229, 2021.

[20] Ashish Vaswani, Noam Shazeer, Niki Parmar, Jakob Uszkoreit, Llion Jones, Aidan N. Gomez, Lukasz Kaiser, and Illia Polosukhin. Attention is all you need. In *Advances in Neural Information Processing Systems 30: Annual Conference on Neural Information Processing Systems 2017, December 4-9, 2017, Long Beach, CA, USA*, pages 5998–6008, 2017.